iScience

Article

PET imaging of HIV-1 envelope protein gp120 using ^{18}F-labeled nanobodies

Graphical abstract

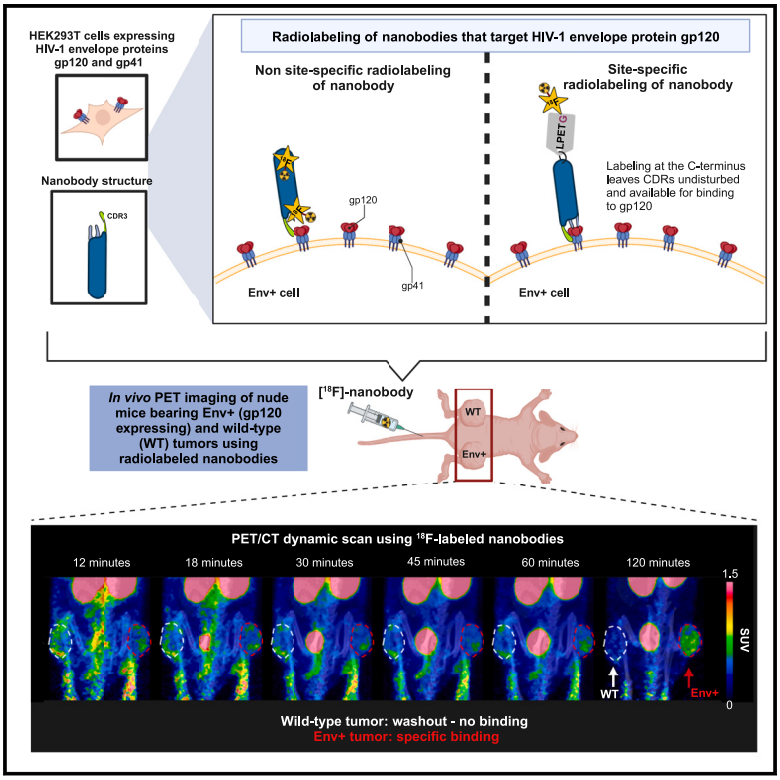

Highlights

- Nanobodies, natural camelid small antibody products, can be used as PET tracers
- Nanobodies against HIV protein gp120 were radiolabeled and evaluated in mice models
- Site-specific ^{18}F-radiolabeling improved tracer binding to gp120 positive tumors
- ^{18}F-labeled J3 nanobody was identified as best candidate for imaging gp120

Authors

Neysha Martinez-Orengo, Swati Shah, Jianhao Lai, ..., Avindra Nath, Chuen-Yen Lau, Dima A. Hammoud

Correspondence

lauc@mail.nih.gov (C.-Y.L.), hammoudd@cc.nih.gov (D.A.H.)

In brief

Immunology; Radiology

Martinez-Orengo et al., 2025, iScience *28*, 111795
February 21, 2025 Published by Elsevier Inc.
https://doi.org/10.1016/j.isci.2025.111795

CellPress

iScience

CellPress
OPEN ACCESS

Article

PET imaging of HIV-1 envelope protein gp120 using ^{18}F-labeled nanobodies

Neysha Martinez-Orengo,[1,7] Swati Shah,[1,7] Jianhao Lai,[1,7] Falguni Basuli,[2] Anna Lyndaker,[1] Mitchell L. Turner,[1] Morteza Peiravi,[1] Suman Sourabh,[1] Kevon Sampson,[3] Peng Zhang,[4,6] Rolf E. Swenson,[2] Paolo Lusso,[4] Frank Maldarelli,[5] Avindra Nath,[3] Chuen-Yen Lau,[5,*] and Dima A. Hammoud[1,8,*]

[1]Center for Infectious Disease Imaging (CIDI), Radiology and Imaging Sciences, Clinical Center (CC), National Institutes of Health, Bethesda, MD, USA

[2]Chemistry and Synthesis Center, National Heart, Lung, and Blood Institute (NHLBI), National Institutes of Health, Rockville, MD, USA

[3]Division of Neuroimmunology and Neurovirology, National Institute of Neurological Disorders and Stroke (NINDS), National Institutes of Health, Bethesda, MD, USA

[4]Laboratory of Immunoregulation, National Institute of Allergy and Infectious Diseases (NIAID), National Institutes of Health, Bethesda, MD, USA

[5]HIV Dynamics and Replication Program, Center for Cancer Research, National Cancer Institute (NCI), National Institutes of Health, Bethesda, MD, USA

[6]Present address: Institute of Health and Medicine, Hefei Comprehensive National Science Center, Hefei 230031, China

[7]These authors contributed equally

[8]Lead contact

*Correspondence: lauc@mail.nih.gov (C.-Y.L.), hammoudd@cc.nih.gov (D.A.H.)

https://doi.org/10.1016/j.isci.2025.111795

SUMMARY

Radiolabeled antibodies against the HIV-1 envelope protein, gp120, have been previously tested in animal models and in people with HIV (PWH). Nanobodies offer advantages over antibodies, including smaller size and faster clearance, which allow labeling with fluorine-18. In this study, three nanobodies (J3, 3E3, B9) chosen based on their binding properties to the conserved CD4-binding site of gp120 were labeled with fluorine-18 and used for PET imaging in mice bearing wild-type (WT) and/or gp120-expressing (Env+) tumors. [^{18}F]J3 and [^{18}F]3E3 selectively targeted Env+ tumors and not WT tumors, with minimal background signal. Switching from non-site-specific radiolabeling method to sortase A-mediated site-specific conjugation at the C-terminus improved binding to Env+ tumors for all nanobodies. Site-specifically ^{18}F-labeled J3 nanobody is the most promising candidate with the highest level of binding. These results establish an Env+ imaging method that will enable next stage testing in an HIV-1 preclinical infection model and potentially in PWH.

INTRODUCTION

Human immunodeficiency virus type-1 (HIV-1) replication can be effectively controlled with antiretroviral therapy (ART). However, latent HIV-1 persists in long-lived infected cells (e.g., CD4$^+$ T cells, macrophages), in peripheral lymphoid tissues and in central nervous system (CNS) microglia of people with HIV (PWH).[1] These HIV-1 reservoirs prevent complete eradication of the virus, and latent proviral DNA can re-activate to produce virions and perpetuate cycles of infection upon ART interruption.[2]

Current approaches for HIV cure include strategies to completely eradicate (sterilizing) or effectively neutralize (functional cure) HIV[3,4]; any approach will require sensitive detection of residual HIV, not simply in blood but in tissue as well. The molecular imaging toolbox for HIV-1 evaluation at the whole-body level includes positron emission tomography (PET) tracers that provide important information about cellular metabolic activity, cellular activation, ART toxicity, immune cell distribution, neurologic complications, and cardiovascular disease, among others.[5–12] More targeted imaging approaches have been used to localize regions of viral persistence and quantify burden of infection. Examples include the use of [^{64}Cu]7D3, a monoclonal antibody targeting simian immunodeficiency virus (SIV) gp120 in macaques and [^{89}Zr]VRC01, a broadly neutralizing monoclonal antibody that targets the CD4 binding site of HIV-1 gp120, in humans, demonstrating that PET is a promising noninvasive approach for the identification of anatomical regions with viral persistence/re-activation in real time.[13,14]

Radiolabeled monoclonal antibodies (mAbs), however, have limitations mostly due to their Fc-dependent non-specific binding and large size, resulting in increased circulation times and the need for using long half-life isotopes, such as zirconium-89 ($t_{1/2}$ = 78.4 h) and copper-64 ($t_{1/2}$ = 12.7 h).[15] Nanobodies, on the other hand, are smaller (~15 kDa compared to ~150 kDa for mAbs) heavy chain-only antibodies that are naturally derived from camelids and are characterized by high antigen-binding affinity, low immunogenicity, thermal stability, and straightforward

synthesis.[16,17] These characteristics enable deep tissue penetration, homogeneous distribution, and quick clearance. Perhaps the most important advantage of using nanobodies is their shorter serum half-life which allows the convenient use of short half-life radioisotopes such as fluorine-18 ($t_{1/2}$ = 109.7 min).[18] With fluorine-18, more frequent longitudinal imaging of the acute/subacute phases of the infection and viral reactivation can be performed, compared to ^{89}Zr-labeled antibodies, for example, where waiting for the equivalent of seven half-lives decay prohibits a close temporal evaluation of the infectious process. This would be extremely valuable in SHIV infected monkeys, for example, where pre-infection imaging can be followed by multiple imaging sessions covering the early stages of the infection and revealing dynamic temporal and spatial progression of the infection. The same imaging can be performed following treatment to demonstrate the decline in gp120 expression in different anatomic compartments until suppression is achieved. During this period, residual binding in various organs compared to pre-infection scans might help identify sites of viral persistence. Similarly, closer imaging time-points enabled by ^{18}F-labeled nanobodies to HIV-1 would facilitate evaluation of viral reactivation sites during human treatment interruption studies.

Radiolabeled nanobodies have been used in preclinical, translational, and even theranostic applications in cancer, with proven superior quality and improved clinical outcomes compared to full antibodies.[16,19–21] No such work has been reported yet for the use of nanobodies to image HIV-1 despite the fact that nanobodies with broad neutralizing capacity of various HIV-1 strains are available.[22–25]

The HIV envelope consists of two subunits, gp41 and gp120, and is organized in the form of a trimer. Upon infection, the gp120 subunit interacts with the CD4 receptor on the host cell to mediate the first step in HIV-1 entry.[26] Here, we investigated the potential of gp120-specific nanobodies as effective radiotracers of gp120 expression *in vitro* and *in vivo*. Three nanobodies (J3, 3E3, and B9), which are known to neutralize 77–96% of tested HIV-1 strains by binding to gp120,[22–25] were labeled with fluorine-18 using two approaches. The first approach was non-site-specific labeling with a prosthetic group targeting various lysines of the nanobody. The second method was site-specific labeling at the C-terminus of the nanobody using sortase A (SrtA)-mediated conjugation, with the aim of preserving the ability of the complementarity-determining regions (CDRs) to bind to their target.

To test the ability of the above-listed radiolabeled nanobodies to image gp120 *in vivo*, we used an Env-expressing HEK293T cell line (Env+) to induce flank tumors in nude mice. As with HIV-infected cells and virions, these Env+ cells express the trimeric form of the HIV-1 envelope glycoprotein on their surface, including the subunit gp120, which is the target antigen of the nanobodies evaluated in this study. The wild-type (WT) HEK293T cell line was used as a control. The tumor-bearing animals underwent dynamic and static PET/CT imaging to monitor the distribution and presence of specific binding *in vivo*. Our goal was to identify the optimal nanobody and radiolabeling strategy (non-site-specific vs. site-specific) to image gp120 expression *in vivo*.

RESULTS

Fluorine-18 radiolabeled nanobodies are produced with high radiochemical purity

Nanobodies were radiolabeled either non-specifically or via site-specific methods. For the non-site-specific method, indirect labeling was done using a prosthetic group that targets the epsilon amino group of lysine residues to produce [^{18}F]nanobody. The overall radiochemical yields were 10–15% (n = 15, decay-corrected) in 50 min. The radiochemical purity was >98% with average specific activity (all scanned animals) of 452 ± 372 Ci/mmol. A representative high-performance liquid chromatogram (HPLC) of [^{18}F]J3 is presented in Figure S1A.

For the site-specific method, SrtA mediated labeling at an LPETG motif on the C-terminus of the nanobody was performed[27] to generate [^{18}F]sortag-nanobody. As a result of the terminal-based labeling, the CDRs of the nanobody remain undisturbed and available for binding to the target. The anticipated outcome is a reduction of background activity and preservation of epitope function.[28] The overall radiochemical yields were 25–40% (n = 12, decay-corrected) in 50 min. The radiochemical purity was >98% with average specific activity (all scanned animals) of 498 ± 172 Ci/mmol. A representative HPLC of [^{18}F]sortag-J3 is presented in Figure S1B.

J3 and 3E3 nanobodies have high binding affinities to the CD4-binding site of gp120

Bio-layer interferometry (BLI) was used to ascertain the binding affinities of the J3, 3E3, and B9 nanobodies with or without the sortag (LPETG motif), since it has been shown that high-affinity binders (lower K_D) are more efficient in targeting tumors *in vivo* compared to those with lower binding.[29] It was also important to confirm that nanobody modification (addition of LPETG motif) for the purposes of sortagging does not negatively affect the binding affinities of the corresponding nanobodies.[30,31] Based on the BLI graphs showing the association and dissociation curves of different concentrations of nanobodies to gp120, the association and dissociation rate constants (k_{on} and k_{off}) are then derived from the fitting curves. Finally, the K_D values are calculated as the quotient of k_{off} and k_{on} (k_{off}/k_{on}).

The K_D values of J3, LPETG-J3, 3E3, LPETG-3E3, B9, and LPETG-B9 were all in the low nanomolar range. The average K_D values (nM) for each nanobody listed above were 1.12, 1.92, 3.33, 2.51, 23.7, and 18.7, respectively. J3 and LPETG-J3 demonstrated higher binding affinities than the rest of the tested nanobodies whereas B9 had approximately 10 times lower binding affinity than J3 and 3E3 (Figure S2A).

To evaluate the two radiolabeling techniques, competition binding assays were performed using non-site specifically labeled J3 ([^{18}F]J3) and site-specifically labeled (sortagged) J3 ([^{18}F]sortag-J3) with the gp120 protein and the Env+ cells. Using the gp120 protein, binding assay curves for [^{18}F]J3 and [^{18}F]sortag-J3 were not appreciably different with comparable IC_{50} values (5.30 nM for [^{18}F]J3 and 3.27 nM for [^{18}F]sortag-J3) across the different concentrations of gp120 (Figure S2B). With the Env+ cells, competition binding assays showed IC_{50} values of 20.96 nM for [^{18}F]J3 and 12.49 nM for [^{18}F]sortag-J3 (Figure S2C).

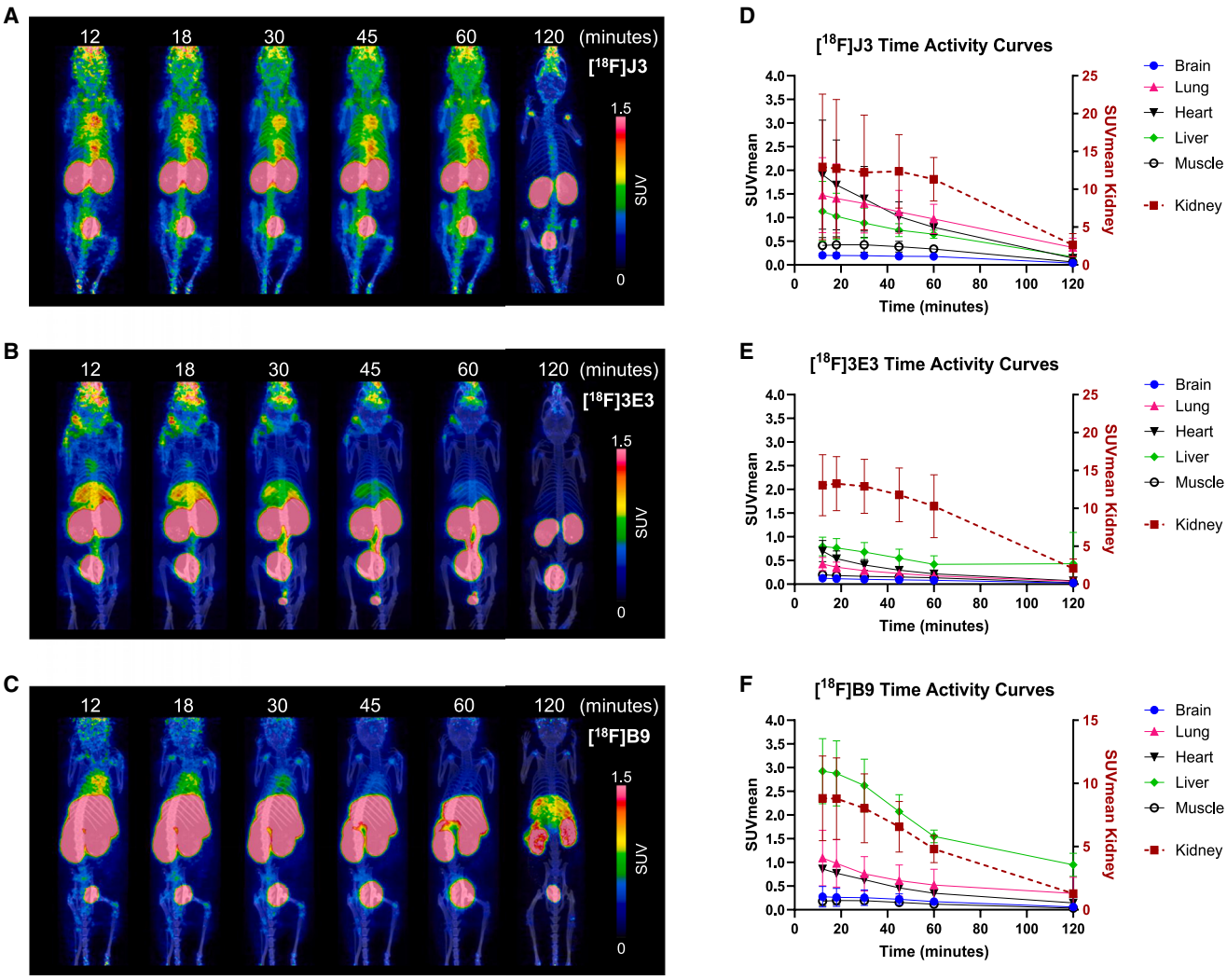

Figure 1. Biodistribution of non-site-specifically labeled nanobodies in control mice

(A–C) Representative PET/CT dynamic (1–60 min) and static scan (at 120 min) for each nanobody: (A) [^{18}F]J3 (n = 5), (B) [^{18}F]3E3 (n = 4), and (C) [^{18}F]B9 (n = 2). (D–F) Time activity curves are shown for the kidneys, brain, lungs, heart, liver, and muscle. Error bars reflect standard deviation (SD) values. Also see Figure S1A for details related to non-specific radiolabeling of the nanobodies.

In both sets of experiments, however, the IC_{50} values were lower for [^{18}F]sortag-J3 compared to [^{18}F]J3, which suggests that specific radiolabeling at the C-terminus slightly improves binding to gp120, likely due to lack of interference of the isotope and prosthetic group with the CDRs.

Immunostaining confirms gp120 expression in cell line and Env+ tumors

Immunofluorescence staining was performed to assess gp120 expression in the cell lines and later in the implanted tumors. We used the well-established gp120 antibody, VRC01, as well as our most promising nanobody, J3. First, fluorescent signal was shown in Env+ cells stained with VRC01 (gp120) and counterstained with DAPI (nucleus) while WT cells were not immunoreactive (Figure S3A). After PET/CT imaging sessions were completed, the mice were euthanized, and their tumors collected and stained. Env+ tumors showed gp120 expression using VRC01, although heterogeneously, especially in larger tumors, while WT tumors were not immunoreactive (Figure S3B). In addition, J3 showed specific staining of gp120 in Env+ tumors that colocalized with VRC01 antibody signal, with no immunoreactivity seen in the WT tumors, as expected, further indicating the specificity of J3 for gp120 protein (Figure S3C).

In vivo [^{18}F]J3 and [^{18}F]3E3, but not [^{18}F]B9, clear from the background by 120 min

When developing new radiotracers, an important step is to assess the pharmacokinetics of the radiotracer. Molecular size/weight and conjugation/labeling methods are some of the factors that affect *in vivo* biodistribution of radiotracers. Smaller molecules (in this case nanobodies) have faster clearance than

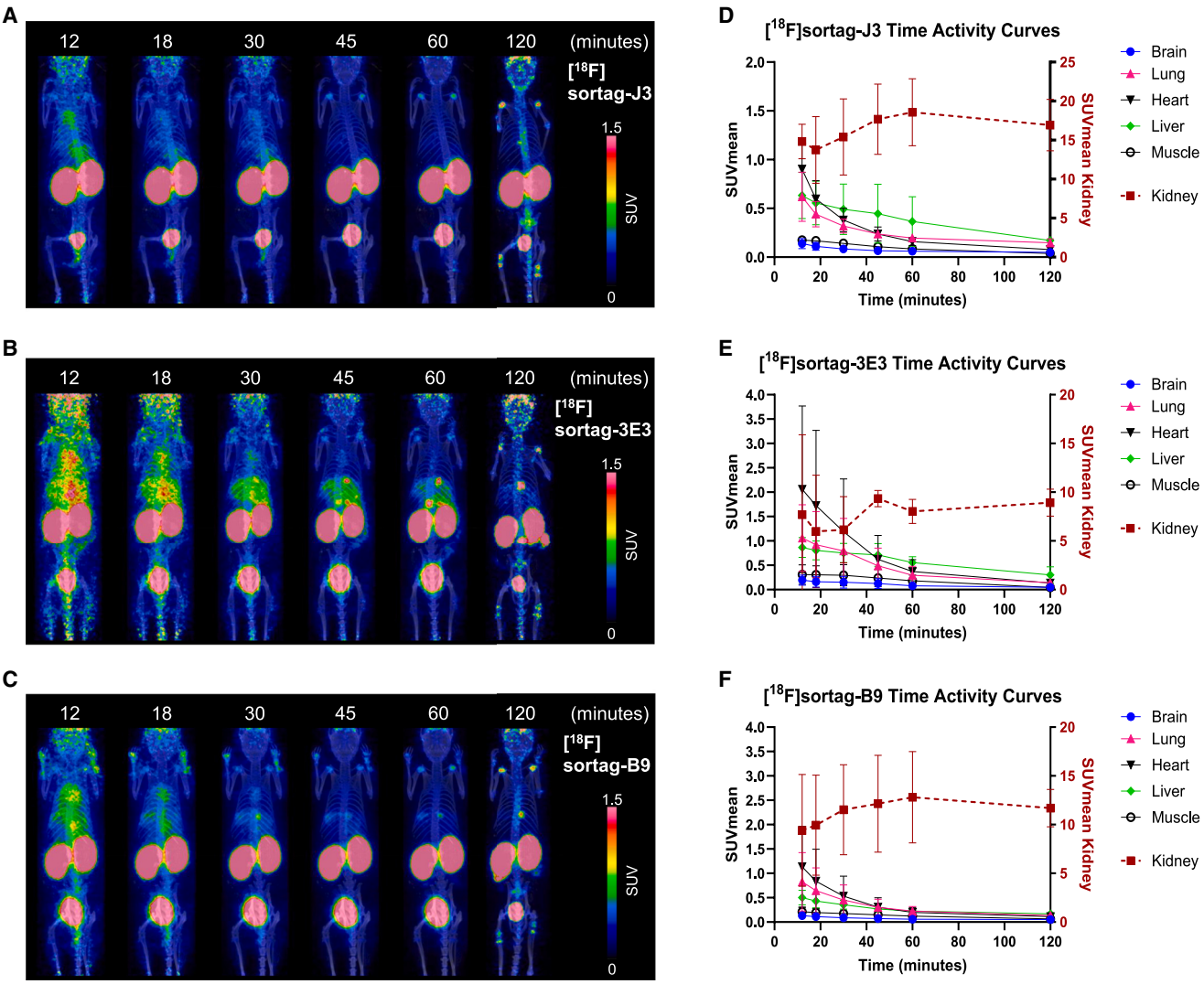

Figure 2. Biodistribution of site-specifically labeled nanobodies in control mice

(A–C) Representative PET/CT dynamic (1–60 min) and static scan (at 120 min) for each nanobody: (A) [^{18}F]sortag-J3 (n = 3), (B) [^{18}F]sortag-3E3 (n = 2), and (C) [^{18}F]sortag-B9 (n = 3).

(D–F) Time activity curves are shown for the kidneys, brain, lungs, heart, liver, and muscle. Error bars reflect standard deviation (SD) values. Also see Figure S1B for details related to site-specific radiolabeling of the nanobodies.

larger ones (e.g., antibodies) allowing the use of shorter half-life isotopes, such as fluorine-18, which results in earlier imaging time points. Different conjugation methods, such as random (targeting lysines) or site-specific labeling (targeting N- or C-terminus) can also affect the biodistribution and clearance of the nanobodies.

Here, healthy mice underwent 60 min dynamic scans followed by static scans at ~120 min after injection of the radiolabeled nanobodies. Organ time activity curves (TACs) with mean standardized uptake values (SUVmean) showed that [^{18}F]J3 and [^{18}F]3E3 were renally excreted and cleared from the background by 120 min. In contrast, [^{18}F]B9 showed high residual background signal especially in the liver and kidneys, both decreasing slowly over 120 min (Figure 1).

Organ time activity curves (TACs) for the site-specifically labeled nanobodies showed faster clearance of background signal compared to the original nanobodies, including [^{18}F]sortag-B9, which showed better clearance than [^{18}F]B9. All the site-specifically labeled nanobodies, however, showed higher kidney retention compared to the non-site-specifically labeled nanobodies as depicted at 120 min following injection (Figure 2).

[^{18}F]J3 and [^{18}F]3E3, but not [^{18}F]B9, show higher binding in Env+ tumors compared to WT tumors

The Env+ tumor model used in our study allowed us to noninvasively compare the performance of the various radiolabeled nanobodies and their labeling methodology, so that the best combination of nanobody and labeling strategy can be further

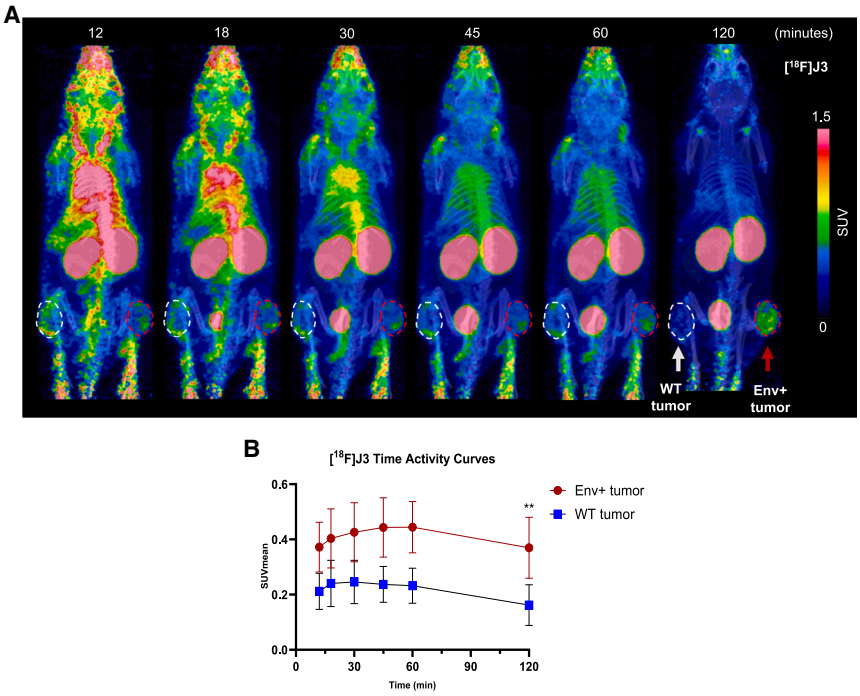

Figure 3. Dynamic and static PET/CT imaging of mice with WT and Env+ tumors using [^{18}F]J3 nanobody

(A) Dynamic PET/CT scan up to 60 min followed by a static 120-min scan of [^{18}F]J3 nanobody in a nude mouse with wild-type (left) and Env+ (right) tumors.

(B) Time activity curves of Env+ (n = 10) vs. wild-type tumor (n = 6) are shown. *Ex vivo* immunofluorescent staining confirmed gp120 expression in Env+ tumors (Figure S3). Error bars reflect standard deviation (SD) values. Unpaired t-test for the 120 min time point, $^{**}p$ = 0.0011.

tested and eventually used to assess gp120 expression in more relevant infectious models such as SHIV-infected monkeys and PWH.

In this study, using dynamic [^{18}F]J3 PET/CT imaging, the WT tumors showed initial non-specific radioactive signal, due to increased vascularity and enhanced permeability and retention (EPR) effect associated with tumors.[32] The unbound radiotracer eventually washed out of the WT tumors over the course of 2 h. On the other hand, the radioactive signal in Env+ tumors continued to increase over time with SUV values at 60 min being lower than SUV values at 120 min in most animals. This indicates a cumulative specific binding of the ligand in tumors with gp120 protein expression rather than delayed washout. Average TACs from both types of tumors are shown in Figure 3.

On the delayed static scans, we elected to use SUVpeak defined by calculating the mean SUV in a sphere with a diameter of 1 mm within the tumor region with the highest activity, instead of SUVmean, to account for the heterogeneity of some tumors as far as gp120 expression. The highest SUVpeak values were seen on images obtained approximately 2 h after tracer injection. [^{18}F]J3 and [^{18}F]3E3 showed significantly higher SUVpeak values in Env+ tumors compared to WT tumors, while [^{18}F]B9 PET showed no significant difference in binding between Env+ and WT tumors (Figure 4). As such, [^{18}F]B9 which has much lower affinity to gp120 than J3, can be potentially considered a negative control nanobody, further supporting the specificity of binding of [^{18}F]J3 and [^{18}F]3E3 to gp120.

When comparing the three nanobodies, there was no significant difference in SUVpeak values between [^{18}F]J3 and [^{18}F]3E3; however, both had significantly higher SUVpeak values compared to [^{18}F]B9 (one-way ANOVA with Tukey's multiple comparison tests; $p < 0.0001$ for both) (Figure S5A).

Site-specifically labeled nanobodies show higher binding in Env+ tumors than non-site-specifically labeled nanobodies

The site-specifically labeled nanobodies exhibited higher SUVpeak values compared to the respective non-site-specifically labeled nanobodies in Env+ tumors. Those differences were statistically significant between [^{18}F]sortag-3E3 and [^{18}F]3E3, and between [^{18}F]sortag-B9 and [^{18}F]B9. Even though there was improved binding for [^{18}F]sortag-J3 compared to [^{18}F]J3, the differences were not statistically significant (Figure 5). Among all nanobodies, [^{18}F]B9 and [^{18}F]sortag-B9 had the lowest SUVpeak values in the Env+ tumors. No binding was observed in the WT tumors with the site-specifically labeled nanobodies (Figure S4).

No significant differences in SUVpeak values between [^{18}F]sortag-J3 and [^{18}F]sortag-3E3 were detected, however, they both showed higher SUVpeak values compared to [^{18}F]sortag-B9 (Figure S5B). Site-specific labeling of B9 increased its binding to gp120 but this was not enough for [^{18}F]sortag-B9 to outperform [^{18}F]sortag-J3 or [^{18}F]sortag-3E3.

DISCUSSION

ImmunoPET is a powerful non-invasive imaging tool that has been previously used to better understand the pathogenesis of HIV-1 infection *in vivo* and more recently, to visualize HIV-1 reservoirs in animal models and in PWH.[13,14] Nanobodies, which are naturally produced by camelids, maintain the antigen targeting properties of antibodies without the inherent limitations of the latter, such as large size, prolonged circulation time and non-specific Fc interactions. In this study, we radiolabeled three nanobodies that target the CD4-binding site of gp120 and tested their ability to selectively visualize gp120 expression *in vivo* in a mouse model. Specific binding of the radiolabeled J3 and 3E3 nanobodies to Env+ tumors but not to WT tumors was demonstrated, and improved binding of J3 and 3E3 was seen when

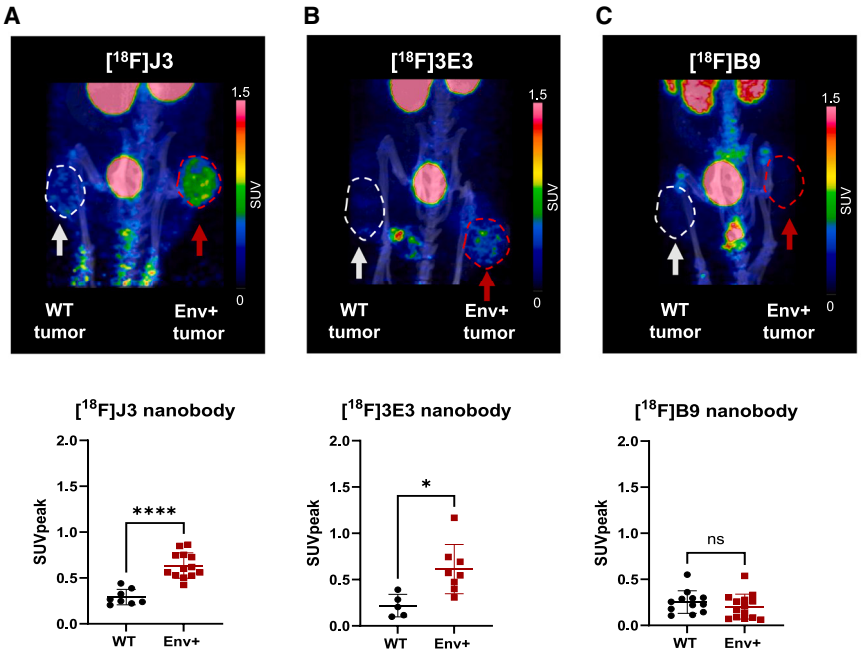

Figure 4. Static PET/CT imaging of mice with WT and Env+ tumors using [^{18}F]J3, [^{18}F]3E3, and [^{18}F]B9 nanobodies

Static 120 min PET/CT scans of nude mice with Env+ (right) and wild-type (left) tumors were performed after administration of [^{18}F]J3 (Env+ $n = 13$, WT $n = 8$), [^{18}F]3E3 (Env+ $n = 8$, WT $n = 5$), or [^{18}F]B9 (Env+ $n = 14$, WT $n = 12$) nanobodies. SUVpeak values in Env+ tumors are significantly higher than values in WT tumors with (A) [^{18}F]J3 and (B) [^{18}F]3E3 but not with (C) [^{18}F]B9 nanobody. Error bars reflect standard deviation (SD) values. Unpaired t-test, ****$p < 0.0001$, *$p = 0.01$, ns = not significant. Binding of non-site-specifically labeled nanobodies [^{18}F]J3 and [^{18}F]3E3 to Env+ tumors is significantly higher than with [^{18}F]B9 (Figure S5A).

using site-specific radiolabeling at the C-terminal of the nanobodies compared to non-site-specific radiolabeling.

Persistence of HIV in reservoirs represents a major hurdle to curing HIV infection. Those reservoirs can be hidden from the immune system, are not eradicated by ART, and reactivate following ART interruption.[1] This is why targeting HIV-1 viral proteins using radiolabeled antibodies (immunoPET) has been previously attempted. One study utilized ^{64}Cu-labeled 7D3, an antibody developed against the CCR5 co-receptor-binding site of gp120, in SIV-infected non-human primates.[13] PET imaging showed higher levels of radioactivity in the gastrointestinal and respiratory tract, lymphoid tissues, and reproductive organs of viremic macaques compared to control uninfected animals while in ART-suppressed macaques and elite controllers there was reduced binding.[13] A similar antibody-based approach was translated in a first-in-human immunoPET study using a ^{89}Zr-labeled version of VRC01, a broadly neutralizing antibody that binds to a highly conserved region of the CD4-binding site of gp120. Increased ^{89}Zr-VRC01 binding was reported in lymph nodes, gut, bone marrow, and nasal turbinates of viremic and suppressed PWH compared to seronegative controls, while inguinal lymph nodes' binding significantly and positively correlated with tissue levels of HIV-1 Gag p24 protein expression.[14] Unlike full antibodies, however, nanobodies have the advantage of shorter circulation time, allowing radiolabeling with short-lived isotopes such as fluorine-18 ($t_{1/2}$ = 109.7 min) compared to isotopes typically used for labeling full antibodies such as zirconium-89 ($t_{1/2}$ = 78.4 h) or copper-64 ($t_{1/2}$ = 12.7 h). Additional advantages of nanobodies include better access to the target antigen due to small size and the ability to form a complex with high-affinity interaction due to longer CDR3 compared to full antibodies.[33] Nanobodies also have fast clearance, high stability, and easy synthesis in prokaryotic cells. The latter results in nanobodies being relatively simple to engineer, so that functionality and sensitivity can be further improved by using multimerizing approaches (e.g., bivalent, trivalent nanobodies) and targeting different epitopes via multiple simultaneous interactions.[34] Nanobodies also share more than 80% sequence homology with human VH3 framework resulting in low immunogenicity,[35] which facilitates clinical translation and longitudinal use. These characteristics enable deep tissue penetration, homogeneous distribution, and quick clearance of nanobodies. Most importantly, as previously mentioned, using shorter half-life fluorine-18, we expect the chosen nanobody, J3, to provide a more dynamic evaluation of the acute and subacute phases of the infection and reactivation in animal models such as SHIV-infected monkeys, and in PWH during analytic treatment interruption compared to full antibodies. Identifying patterns of increased binding after infection and decreased binding after treatment in animals might reveal anatomic sites with residual HIV-infected cells during viral suppression. A similar assessment of the reactivation dynamics and spatial distribution of viral spread could potentially be performed in PWH after treatment interruption while the dynamics of viral control can be subsequently evaluated upon resumption of treatment.

All three nanobodies used in our study (J3, 3E3, and B9) are known to bind the CD4-binding site of gp120 [22,24,36,37] with different degrees of HIV-1 neutralization (96%, 95%, and 77% for J3, 3E3, and B9, respectively).[25] Nanobodies typically have three CDRs. J3 and 3E3, which showed the best results in our hands, share certain CDR characteristics, including lack of three residues in the CDR2 as a result of affinity maturation, compared to their respective germline sequence, which influence their binding abilities.[24] Additionally, the footprint of J3 is very similar to that of CD4 and has degrees of maturation outside its paratope, which could improve affinity.[24,37] Thus, J3 can mimic the interaction between the CD4 receptor and the CD4 binding site of HIV-1 gp120. The latter might account, at least partially, for slightly better performance of J3 compared to 3E3 in our study. Furthermore, the synthesis of J3 is more feasible with an overall yield around 20-fold higher than that of 3E3 synthesis.

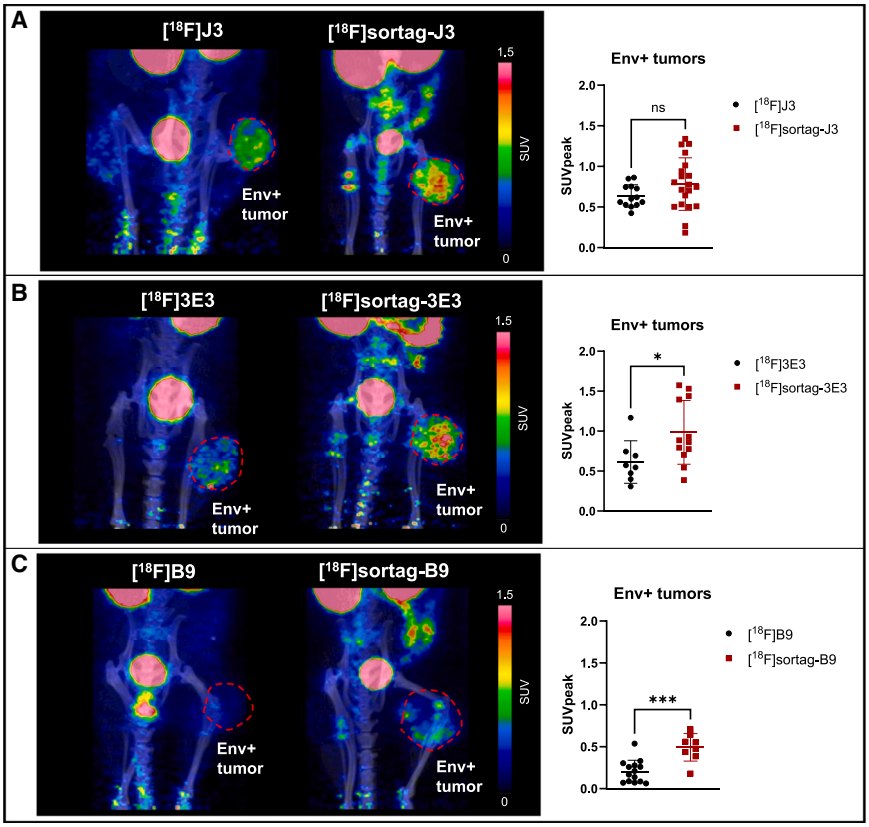

Figure 5. Static PET/CT imaging of mice with Env+ tumors using non-site-specifically and site-specifically labeled nanobodies

(A–C) Static 120 min PET/CT scans of nude mice with Env+ tumors performed after administration of (A) [^{18}F]J3 (n = 13) and [^{18}F]sortag-J3 (n = 20), (B) [^{18}F]3E3 (n = 8) and [^{18}F]sortag-3E3 (n = 12), and (C) [^{18}F]B9 (n = 14) and [^{18}F]sortag-B9 (n = 8). Binding of the nanobodies to the Env+ tumor (SUVpeak values) is higher with site-specifically labeling compared to non-site-specifically labeling, and statistically significant in 3E3 and B9 nanobodies. Error bars reflect standard deviation (SD) values. Unpaired t-test, ***p = 0.0002, *p = 0.03, ns = not significant. Binding of site-specifically labeled nanobodies [^{18}F]sortag-J3 and [^{18}F]sortag-3E3 to Env+ tumors is higher than with [^{18}F]sortag-B9 (Figure S5B).

Radiolabeled nanobodies are widely utilized in oncology imaging applications and in other fields due to their high signal to background ratio. Modifications to the radiolabeling procedures of nanobodies can further expand their imaging and diagnostic capabilities. The epsilon amino group of lysine residues is commonly used for the conjugation of chelators or prosthetics groups.[18] However, these non-site-specific conjugations have the potential of altering the availability of the antigen binding site if they engage lysine residues within or in close proximity to the CDRs.[18,38] An alternative aimed at preserving the ability of the CDRs to bind to their targeted antigen is a site-specific labeling strategy using sortase A (SrtA) mediated site-specific conjugation. In our hands, we saw increased binding of [^{18}F]sortag-3E3 and [^{18}F]sortag-B9 to Env+ tumors compared to [^{18}F]3E3 and [^{18}F]B9. We also found higher SUVpeak values in Env+ with [^{18}F]sortag-J3 compared to [^{18}F]J3, though the difference was not statistically significant with our sample number.

The HIV envelope protein, gp120, is present at higher levels in viremic PWH compared to those on effective ART.[39] As a result, the radiolabeled nanobody will probably be most useful in characterizing reactivation dynamics and localizing sites of reactivation prior to viral repopulation of the periphery following ART cessation. In this regard, evaluation of current HIV cure strategies will greatly benefit from the high sensitivity of PET and the short half-life of fluorine-18 allowing close and frequent assessment of gp120 expression as a proxy for viral activity.

In conclusion, we have developed ^{18}F-labeled gp120-binding nanobodies with potential for noninvasive identification and assessment of gp120 expression on HIV-infected cells *in vivo*. Based on affinity, labeling method, pharmacokinetics and level of *in vivo* binding signal from HIV-1 Env+ tumors compared to WT tumors, we established that site-specifically labeled J3 ([^{18}F]sortag-J3) is the best performing nanobody candidate for imaging gp120 *in vivo*. Further evaluation of [^{18}F]sortag-J3 will be pursued in SHIV infected macaques during the acute and sub-acute phases of the infection and eventually, in PWH undergoing ART interruption and resumption studies. If successful, noninvasive dynamic *in vivo* characterization of HIV-1 viral activity through gp120 expression could potentially be used in conjunction with HIV-1 cure strategies under evaluation.[40]

Limitations of the study

Even though our tumor model is similar in size to a human lymph node, it has high and localized gp120 expression and therefore does not reflect the natural distribution of gp120 expression in infected animals or patients. In addition, levels of gp120 expression in infected animals and humans vary across various organs and depend on viral load and response to treatment. However, this limitation is not specific to our approach and is theoretically more concerning with larger antibodies. Another potential limitation is the high renal retention of the radiolabeled nanobodies, especially the site-specifically labeled ones. This might depend on the number of polar residues in the C-terminal amino acid tag, as studies comparing Myc-His-tagged, His-tagged, and untagged radiolabeled nanobodies showed near 90% lower renal retention with the untagged tracer.[41] In our case, however, the sortagged nanobody (without His-tag) had higher kidney retention than the non-site specific labeled nanobody (with His-tag), suggesting there are other factors involved in determining renal excretion. To overcome the challenge of nanobodies

accumulating in the kidneys, additional strategies are being developed, including injections with positively charged amino acids, and the attachment of smaller PEG moieties.[17] We are planning on testing those strategies with [^{18}F]sortag-J3 to decrease renal retention.

RESOURCE AVAILABILITY

Lead contact

Further information and requests for resources and reagents should be directed to and will be fulfilled by the lead contact, Dima A. Hammoud (hammoudd@cc.nih.gov).

Materials availability

The sequences of the tested nanobodies[22,36] and the radiolabeling methodology have been published[27] and can be reproduced. The sequences for the sortagged nanobodies used in this study can be accessed in Mendeley Data: https://doi.org/10.17632/7ff2cbxk5v.1.

Data and code availability

- All data supporting the findings of this study can be shared by the lead author Dima A. Hammoud upon request.
- No original code was generated for this study.
- Any additional information required to reanalyze the data reported in this paper is available from the lead contact upon request.

ACKNOWLEDGMENTS

This research was supported by the Office of AIDS Research (OAR) and by the NIH Intramural Research Program of the Clinical Center (Center for Infectious Disease Imaging, Radiology and Imaging Sciences), the National Cancer Institute (Center for Cancer Research) and the National Institute of Neurological Disorders and Stroke.

The plasmids for the J3, 3E3, and B9 nanobodies to the HIV-1 gp120 CD4 binding site were graciously provided by Dr. Laura McCoy (Institute of Immunity and Transplantation, Division of Infection and Immunity, University College London, England, UK). The following reagents were obtained through the NIH HIV reagent program, division of AIDS, NIAID, NIH: monoclonal anti-human immunodeficiency virus (HIV)-1 gp120 Protein (VRC01, produced *in vitro*), ARP-12033, contributed by Dr. John Mascola and human immunodeficiency virus type 1 JR-CSF Fc-gp120 protein, recombinant from CHO cells, ARP-11556, contributed by Dr. John Elder and Aymeric de Parseval.

The content of this publication is solely the responsibility of the author(s) and does not necessarily represent the official views of the National Institutes of Health.

AUTHOR CONTRIBUTIONS

D.A.H., C.-Y.L., P.L., F.M., R.E.S, and A.N. conceived and designed the study. F.B. synthesized and tested the radiochemical ligands. N.M.-O., S.S., J.L., A.L., M.L.T., M.P., S.S., K.S., and P.Z. participated in the acquisition and/or analysis of the data. All authors participated in drafting the manuscript and/or revising it critically for intellectual content.

DECLARATION OF INTERESTS

The authors declare no conflicts of interests.

STAR★METHODS

Detailed methods are provided in the online version of this paper and include the following:

SUPPLEMENTAL INFORMATION

Supplemental information can be found online at https://doi.org/10.1016/j.isci.2025.111795.

Received: August 2, 2024
Revised: November 2, 2024
Accepted: January 9, 2025
Published: January 13, 2025

REFERENCES

1. Chen, J., Zhou, T., Zhang, Y., Luo, S., Chen, H., Chen, D., Li, C., and Li, W. (2022). The reservoir of latent HIV. Front. Cell. Infect. Microbiol. *12*, 945956. https://doi.org/10.3389/fcimb.2022.945956.
2. Lau, C.Y., Adan, M.A., and Maldarelli, F. (2021). Why the HIV Reservoir Never Runs Dry: Clonal Expansion and the Characteristics of HIV-Infected Cells Challenge Strategies to Cure and Control HIV Infection. Viruses *13*, 2512. https://doi.org/10.3390/v13122512.
3. Davenport, M.P., Khoury, D.S., Cromer, D., Lewin, S.R., Kelleher, A.D., and Kent, S.J. (2019). Functional cure of HIV: the scale of the challenge. Nat. Rev. Immunol. *19*, 45–54. https://doi.org/10.1038/s41577-018-0085-4.
4. Turk, G., Seiger, K., Lian, X., Sun, W., Parsons, E.M., Gao, C., Rassadkina, Y., Polo, M.L., Czernikier, A., Ghiglione, Y., et al. (2022). A Possible Sterilizing Cure of HIV-1 Infection Without Stem Cell Transplantation. Ann. Intern. Med. *175*, 95–100. https://doi.org/10.7326/L21-0297.
5. Henrich, T.J., Hsue, P.Y., and VanBrocklin, H. (2019). Seeing Is Believing: Nuclear Imaging of HIV Persistence. Front. Immunol. *10*, 2077. https://doi.org/10.3389/fimmu.2019.02077.
6. Patel, R., Manion, M.M., Laidlaw, E., Wakim, P., Wang, Z., Anderson, M., Galindo, F., Rupert, A., Lisco, A., Heller, T., et al. (2022). Improvement of liver metabolic activity in people with advanced HIV after antiretroviral therapy initiation. AIDS *36*, 1655–1664. https://doi.org/10.1097/QAD.0000000000003302.
7. Wang, Z., Manion, M.M., Laidlaw, E., Rupert, A., Lau, C.Y., Smith, B.R., Nath, A., Sereti, I., and Hammoud, D.A. (2021). Redistribution of brain glucose metabolism in people with HIV after antiretroviral therapy initiation. AIDS *35*, 1209–1219. https://doi.org/10.1097/QAD.0000000000002875.
8. Sinharay, S., and Hammoud, D.A. (2019). Brain PET Imaging: Value for Understanding the Pathophysiology of HIV-associated Neurocognitive Disorder (HAND). Curr. HIV AIDS Rep. *16*, 66–75. https://doi.org/10.1007/s11904-019-00419-8.
9. Hammoud, D.A., Boulougoura, A., Papadakis, G.Z., Wang, J., Dodd, L.E., Rupert, A., Higgins, J., Roby, G., Metzger, D., Laidlaw, E., et al. (2019). Increased Metabolic Activity on 18F-Fluorodeoxyglucose Positron Emission Tomography-Computed Tomography in Human Immunodeficiency Virus-Associated Immune Reconstitution Inflammatory Syndrome. Clin. Infect. Dis. *68*, 229–238. https://doi.org/10.1093/cid/ciy454.
10. Sinharay, S., Lee, D., Shah, S., Muthusamy, S., Papadakis, G.Z., Zhang, X., Maric, D., Reid, W.C., and Hammoud, D.A. (2017). Cross-sectional and longitudinal small animal PET shows pre and post-synaptic striatal dopaminergic deficits in an animal model of HIV. Nucl. Med. Biol. *55*, 27–33. https://doi.org/10.1016/j.nucmedbio.2017.08.004.

11. Hammoud, D.A., Sinharay, S., Shah, S., Schreiber-Stainthorp, W., Maric, D., Muthusamy, S., Lee, D.E., Lee, C.A., Basuli, F., Reid, W.C., et al. (2019). Neuroinflammatory Changes in Relation to Cerebrospinal Fluid Viral Load in Simian Immunodeficiency Virus Encephalitis. mBio *10*, e00970-19. https://doi.org/10.1128/mBio.00970-19.

12. Brust, D., Polis, M., Davey, R., Hahn, B., Bacharach, S., Whatley, M., Fauci, A.S., and Carrasquillo, J.A. (2006). Fluorodeoxyglucose imaging in healthy subjects with HIV infection: impact of disease stage and therapy on pattern of nodal activation. AIDS *20*, 985–993. https://doi.org/10.1097/01.aids.0000222070.52996.76.

13. Santangelo, P.J., Rogers, K.A., Zurla, C., Blanchard, E.L., Gumber, S., Strait, K., Connor-Stroud, F., Schuster, D.M., Amancha, P.K., Hong, J.J., et al. (2015). Whole-body immunoPET reveals active SIV dynamics in viremic and antiretroviral therapy-treated macaques. Nat. Methods *12*, 427–432. https://doi.org/10.1038/nmeth.3320.

14. Beckford-Vera, D.R., Flavell, R.R., Seo, Y., Martinez-Ortiz, E., Aslam, M., Thanh, C., Fehrman, E., Pardons, M., Kumar, S., Deitchman, A.N., et al. (2022). First-in-human immunoPET imaging of HIV-1 infection using (89) Zr-labeled VRC01 broadly neutralizing antibody. Nat. Commun. *13*, 1219. https://doi.org/10.1038/s41467-022-28727-5.

15. Chames, P., Van Regenmortel, M., Weiss, E., and Baty, D. (2009). Therapeutic antibodies: successes, limitations and hopes for the future. Br. J. Pharmacol. *157*, 220–233. https://doi.org/10.1111/j.1476-5381.2009.00190.x.

16. Yang, E., Liu, Q., Huang, G., Liu, J., and Wei, W. (2022). Engineering nanobodies for next-generation molecular imaging. Drug Discov. Today *27*, 1622–1638. https://doi.org/10.1016/j.drudis.2022.03.013.

17. Harmand, T.J., Islam, A., Pishesha, N., and Ploegh, H.L. (2021). Nanobodies as *in vivo*, non-invasive, imaging agents. RSC Chem. Biol. *2*, 685–701. https://doi.org/10.1039/d1cb00023c.

18. Kuppers, J., Kurpig, S., Bundschuh, R.A., Essler, M., and Lutje, S. (2021). Radiolabeling Strategies of Nanobodies for Imaging Applications. Diagnostics *11*, 1530. https://doi.org/10.3390/diagnostics11091530.

19. D'Huyvetter, M., De Vos, J., Xavier, C., Pruszynski, M., Sterckx, Y.G.J., Massa, S., Raes, G., Caveliers, V., Zalutsky, M.R., Lahoutte, T., and Devoogdt, N. (2017). (131)I-labeled Anti-HER2 Camelid sdAb as a Theranostic Tool in Cancer Treatment. Clin. Cancer Res. *23*, 6616–6628. https://doi.org/10.1158/1078-0432.Ccr-17-0310.

20. Vaidyanathan, G., McDougald, D., Choi, J., Koumarianou, E., Weitzel, D., Osada, T., Lyerly, H.K., and Zalutsky, M.R. (2016). Preclinical Evaluation of 18F-Labeled Anti-HER2 Nanobody Conjugates for Imaging HER2 Receptor Expression by Immuno-PET. J. Nucl. Med. *57*, 967–973. https://doi.org/10.2967/jnumed.115.171306.

21. Zhou, Z., Meshaw, R., Zalutsky, M.R., and Vaidyanathan, G. (2021). Site-Specific and Residualizing Linker for (18)F Labeling with Enhanced Renal Clearance: Application to an Anti-HER2 Single-Domain Antibody Fragment. J. Nucl. Med. *62*, 1624–1630. https://doi.org/10.2967/jnumed.120.261446.

22. McCoy, L.E., Quigley, A.F., Strokappe, N.M., Bulmer-Thomas, B., Seaman, M.S., Mortier, D., Rutten, L., Chander, N., Edwards, C.J., Ketteler, R., et al. (2012). Potent and broad neutralization of HIV-1 by a llama antibody elicited by immunization. J. Exp. Med. *209*, 1091–1103. https://doi.org/10.1084/jem.20112655.

23. McCoy, L.E., Groppelli, E., Blanchetot, C., de Haard, H., Verrips, T., Rutten, L., Weiss, R.A., and Jolly, C. (2014). Neutralisation of HIV-1 cell-cell spread by human and llama antibodies. Retrovirology *11*, 83. https://doi.org/10.1186/s12977-014-0083-y.

24. Strokappe, N.M., Hock, M., Rutten, L., McCoy, L.E., Back, J.W., Caillat, C., Haffke, M., Weiss, R.A., Weissenhorn, W., and Verrips, T. (2019). Super Potent Bispecific Llama VHH Antibodies Neutralize HIV via a Combination of gp41 and gp120 Epitopes. Antibodies *8*, 38. https://doi.org/10.3390/antib8020038.

25. Weiss, R.A., and Verrips, C.T. (2019). Nanobodies that Neutralize HIV. Vaccines *7*, 77. https://doi.org/10.3390/vaccines7030077.

26. Liu, Q., Acharya, P., Dolan, M.A., Zhang, P., Guzzo, C., Lu, J., Kwon, A., Gururani, D., Miao, H., Bylund, T., et al. (2017). Quaternary contact in the initial interaction of CD4 with the HIV-1 envelope trimer. Nat. Struct. Mol. Biol. *24*, 370–378. https://doi.org/10.1038/nsmb.3382.

27. Basuli, F., Shi, J., Lindberg, E., Fayn, S., Lee, W., Ho, M., Hammoud, D.A., Cheloha, R.W., Swenson, R.E., and Escorcia, F.E. (2024). Sortase-Mediated Site-Specific Conjugation to Prepare Fluorine-18-Labeled Nanobodies. Bioconjugate Chem. *35*, 1335–1342. https://doi.org/10.1021/acs.bioconjchem.4c00264.

28. Pleiner, T., Bates, M., Trakhanov, S., Lee, C.T., Schliep, J.E., Chug, H., Böhning, M., Stark, H., Urlaub, H., and Görlich, D. (2015). Nanobodies: site-specific labeling for super-resolution imaging, rapid epitope-mapping and native protein complex isolation. Elife *4*, e11349. https://doi.org/10.7554/eLife.11349.

29. Viti, F., Tarli, L., Giovannoni, L., Zardi, L., and Neri, D. (1999). Increased binding affinity and valence of recombinant antibody fragments lead to improved targeting of tumoral angiogenesis. Cancer Res. *59*, 347–352.

30. Dewulf, J., Flieswasser, T., Delahaye, T., Vangestel, C., Miranda, A., de Haard, H., Jacobs, J., Smits, E., Van den Wyngaert, T., and Elvas, F. (2023). Site-specific (68)Ga-labeled nanobody for PET imaging of CD70 expression in preclinical tumor models. EJNMMI Radiopharm. Chem. *8*, 8. https://doi.org/10.1186/s41181-023-00194-3.

31. Massa, S., Vikani, N., Betti, C., Ballet, S., Vanderhaegen, S., Steyaert, J., Descamps, B., Vanhove, C., Bunschoten, A., van Leeuwen, F.W.B., et al. (2016). Sortase A-mediated site-specific labeling of camelid single-domain antibody-fragments: a versatile strategy for multiple molecular imaging modalities. Contrast Media Mol. Imaging *11*, 328–339. https://doi.org/10.1002/cmmi.1696.

32. Wu, J. (2021). The Enhanced Permeability and Retention (EPR) Effect: The Significance of the Concept and Methods to Enhance Its Application. J. Personalized Med. *11*, 771. https://doi.org/10.3390/jpm11080771.

33. Liu, B., and Yang, D. (2022). Easily Established and Multifunctional Synthetic Nanobody Libraries as Research Tools. Int. J. Mol. Sci. *23*, 1482. https://doi.org/10.3390/ijms23031482.

34. Misson Mindrebo, L., Liu, H., Ozorowski, G., Tran, Q., Woehl, J., Khalek, I., Smith, J.M., Barman, S., Zhao, F., Keating, C., et al. (2023). Fully synthetic platform to rapidly generate tetravalent bispecific nanobody-based immunoglobulins. Proc. Natl. Acad. Sci. USA *120*, e2216612120. https://doi.org/10.1073/pnas.2216612120.

35. Asaadi, Y., Jouneghani, F.F., Janani, S., and Rahbarizadeh, F. (2021). A comprehensive comparison between camelid nanobodies and single chain variable fragments. Biomark. Res. *9*, 87. https://doi.org/10.1186/s40364-021-00332-6.

36. McCoy, L.E., Rutten, L., Frampton, D., Anderson, I., Granger, L., Bashford-Rogers, R., Dekkers, G., Strokappe, N.M., Seaman, M.S., Koh, W., et al. (2014). Molecular evolution of broadly neutralizing Llama antibodies to the CD4-binding site of HIV-1. PLoS Pathog. *10*, e1004552. https://doi.org/10.1371/journal.ppat.1004552.

37. Zhou, T., Chen, L., Gorman, J., Wang, S., Kwon, Y.D., Lin, B.C., Louder, M.K., Rawi, R., Stancofski, E.S.D., Yang, Y., et al. (2022). Structural basis for llama nanobody recognition and neutralization of HIV-1 at the CD4-binding site. Structure *30*, 862–875.e4. https://doi.org/10.1016/j.str.2022.03.012.

38. Haque, M., Forte, N., and Baker, J.R. (2021). Site-selective lysine conjugation methods and applications towards antibody-drug conjugates. Chem. Commun. *57*, 10689–10702. https://doi.org/10.1039/d1cc03976h.

39. Buck, A.M., Deveau, T.M., Henrich, T.J., and Deitchman, A.N. (2023). Challenges in HIV-1 Latent Reservoir and Target Cell Quantification in CAR-T Cell and Other Lentiviral Gene Modifying HIV Cure Strategies. Viruses *15*, 1126. https://doi.org/10.3390/v15051126.

40. Jean, M.J., Fiches, G., Hayashi, T., and Zhu, J. (2019). Current Strategies for Elimination of HIV-1 Latent Reservoirs Using Chemical Compounds Targeting Host and Viral Factors. AIDS Res. Hum. Retrovir. *35*, 1–24. https://doi.org/10.1089/AID.2018.0153.

41. D'Huyvetter, M., Vincke, C., Xavier, C., Aerts, A., Impens, N., Baatout, S., De Raeve, H., Muyldermans, S., Caveliers, V., Devoogdt, N., and Lahoutte, T. (2014). Targeted radionuclide therapy with A 177Lu-labeled anti-HER2 nanobody. Theranostics *4*, 708–720. https://doi.org/10.7150/thno.8156.

42. Zhang, P., Narayanan, E., Liu, Q., Tsybovsky, Y., Boswell, K., Ding, S., Hu, Z., Follmann, D., Lin, Y., Miao, H., et al. (2021). A multiclade env-gag VLP mRNA vaccine elicits tier-2 HIV-1-neutralizing antibodies and reduces the risk of heterologous SHIV infection in macaques. Nat. Med. *27*, 2234–2245. https://doi.org/10.1038/s41591-021-01574-5.

43. Basuli, F., Zhang, X., Woodroofe, C.C., Jagoda, E.M., Choyke, P.L., and Swenson, R.E. (2017). Fast indirect fluorine-18 labeling of protein/peptide using the useful 6-fluoronicotinic acid-2,3,5,6-tetrafluorophenyl prosthetic group: A method comparable to direct fluorination. J. Label. Compd. Radiopharm. *60*, 168–175. https://doi.org/10.1002/jlcr.3487.

44. Mazmanian, S.K., Liu, G., Ton-That, H., and Schneewind, O. (1999). Staphylococcus aureus sortase, an enzyme that anchors surface proteins to the cell wall. Science *285*, 760–763. https://doi.org/10.1126/science.285.5428.760.

45. Rashidian, M., Keliher, E., Dougan, M., Juras, P.K., Cavallari, M., Wojtkiewicz, G.R., Jacobsen, J., Edens, J.G., Tas, J.M.G., Victora, G., et al. (2015). The use of (18)F-2-fluorodeoxyglucose (FDG) to label antibody fragments for immuno-PET of pancreatic cancer. ACS Cent. Sci. *1*, 142–147. https://doi.org/10.1021/acscentsci.5b00121.

46. Bannas, P., Hambach, J., and Koch-Nolte, F. (2017). Nanobodies and Nanobody-Based Human Heavy Chain Antibodies As Antitumor Therapeutics. Front. Immunol. *8*, 1603. https://doi.org/10.3389/fimmu.2017.01603.

47. Lai, J., Lu, D., Zhang, C., Zhu, H., Gao, L., Wang, Y., Bao, R., Zhao, Y., Jia, B., Wang, F., et al. (2018). Noninvasive small-animal imaging of galectin-1 upregulation for predicting tumor resistance to radiotherapy. Biomaterials *158*, 1–9. https://doi.org/10.1016/j.biomaterials.2017.12.012.

STAR★METHODS

KEY RESOURCES TABLE

REAGENT or RESOURCE	SOURCE	IDENTIFIER
Antibodies		
J3 nanobody	McCoy et al., 2012[22]	https://doi.org/10.1084/jem.20112655
3E3 nanobody	McCoy et al., 2014[36]	https://doi.org/10.1371/journal.ppat.1004552
B9 nanobody	McCoy et al., 2014[36]	https://doi.org/10.1371/journal.ppat.1004552
LPETG sortag-J3 nanobody	GenScript	https://doi.org/10.17632/7ff2cbxk5v.1
LPETG sortag-3E3 nanobody	GenScript	https://doi.org/10.17632/7ff2cbxk5v.1
LPETG sortag-B9 nanobody	GenScript	https://doi.org/10.17632/7ff2cbxk5v.1
[18F]J3	This paper	N/A
[18F]3E3	This paper	N/A
[18F]B9	This paper	N/A
[18F]Sortag-J3	This paper	N/A
[18F]Sortag-3E3	This paper	N/A
[18F]Sortag-B9	This paper	N/A
VRC01	NIH AIDS Reagent Program	ARP-12033
Alexa fluor 647	Invitrogen	Cat# 21445
AlexaFluor 647 anti-His Tag	Biolegend	Cat# 362611
Chemicals, peptides, and recombinant proteins		
Phosphate buffered saline (1X)	Gibco	Cat# 10010-031-1000mL
Bovine Serum Albumin	Sigma	Cat# A9647-100G
Tween 20	Sigma	Cat# 9416-100mL
Dulbecco's Modified Eagle Medium	Gibco	Cat# 11965-092-500mL
Fetal Bovine Serum, heat inactivated	Sigma	Cat# F4135-500mL
Penicillin Streptomycin	Sigma	Cat# P4458-100mL
Paraformaldehyde 32% solution	Electron Microscopy Sciences	Cat# 15714-s
Tris buffered saline (10X)	Crystalgen	Cat# 302-003-1000-1L
TrueVIEW autofluorescence quenching reagent	Vector Labs	Cat# SP-8400
Mounting media containing 4', 6-diamidino-2-phenylindole (DAPI)	Invitrogen	Cat# P36935
DAPI	Invitrogen	Cat# D1306
Sucrose $\geq$99.5%	Sigma	Cat# S8501-5KG
Optimal Cutting Compound	Sakura	Cat# 4583
Fc-gp120 protein	NIH AIDS Reagent Program	ARP-11556
6-fluoronicotinic acid-2,3,5,6-tetrafluorophenyl ester (6-[18F]FPy-TFP)	Basuli et al., 2017[43]	https://doi.org/10.1002/jlcr.3487
Experimental models: Cell lines		
HEK293T wild type cells	Dr. Paolo Lusso	N/A
HEK293T HIV-1 Env+ cells	Dr. Paolo Lusso	N/A
Experimental models: Organisms/strains		
Athymic Nude female mice	Jackson Laboratory	FOXN1NU/NU model #002019
Software and algorithms		
GraphPad Prism 10	GraphPad	https://www.graphpad.com/updates/prism-900-release-notes
Olympus OlyVIA 4.1.1	Olympus	https://www.olympus-lifescience.com/en/downloads/detail-iframe/?0[downloads][id]=847254061

(*Continued on next page*)

Continued

REAGENT or RESOURCE	SOURCE	IDENTIFIER
MIM 7.3.3	MIM	https://www.mimsoftware.com/resources/supplemental-documents#
Octet Analysis Studio 13.0	Sartorius	https://www.sartorius.com/download/552418/octet-data-analysis-ht-software-datasheet-en-sartorius-data.pdf
OSEM-3D	Mediso	https://mediso.com/hungary/en/product/pre-clinical-products/nanoscanr-petct
Other		
BLI Nitrilotriacetic acid (NTA) sensors	Sartorius	Cat# 18-5101
Multiscreen® high binding strip plates	Millipore Sigma	M8CHNFX00

EXPERIMENTAL MODEL AND STUDY PARTICIPANT DETAILS

Cell lines

To generate a stably transfected cell line constitutively expressing high levels of HIV-1 Env, a lentiviral expression plasmid was synthesized by subcloning DNA from a WITO Env clone (WITO.27_1.745)[42] into the pLenti-III-HA vector (pLenti-Env). Lentiviral particles were produced by co-transfecting HEK293T/17 cells with three plasmids (pLenti-Env, a packaging plasmid, psPAX2, and a vesicular stomatitis virus (VSV) G protein-expressing plasmid). Following transduction, the HIV-1 Env DNA became integrated into the genome of HEK293T cells. Transduced cells were expanded in the presence of the selection antibiotic puromycin and sorted by gating on high Env expression, as determined by flow cytometry using the reference antibody 2G12. Sorted cells were then cloned by limiting dilution, and individual clones were expanded, selected, and tested for Env expression over time (Zhang et al., manuscript in preparation). One clone (A6) with stable high Env expression over time was selected for the current experiments. The Env expressed on the cell surface of A6 cells was documented to be predominantly in the native, trimeric form as shown by binding of trimer-specific antibodies such as PGT145 and PGT151. The Env-expressing (A6) and WT HEK293T cells were each cultured in DMEM media (Gibco, Grand Island, NY, USA) supplemented with 10% fetal bovine serum and 1% Penicillin Streptomycin and incubated at 37°C with 5% CO_2 until confluent. All cell lines used in this study were examined by IDEXX BioAnalytics (Columbia, MO) using IMPACT 1 PCR profile which confirmed that cell lines were negative for Corynebacterium bovis, Corynebacterium sp. (HAC2), Ectromelia, EDIM, Hantaan, K virus, LCMV, LDEV, MAV1, MAV2, mCMV, MHV, MNV, Mouse kidney parvovirus (MKPV), MPV, MTV, MVM, Mycoplasma pulmonis, Mycoplasma sp., Polyoma, PVM, REO3, Sendai, TMEV.

Mouse tumor model

For *in vivo* PET imaging, animal models with WT HEK293T and/or Env+ HEK293T flank tumors were developed using 6 to 8-week-old female athymic nude mice FOXN1NU/NU model #002019 (Jackson Laboratory, Bar Harbor, ME, USA). Upon arrival to the animal facility, mice were housed in pre-sterilized filter-topped cages and given access to food and water *ad libitum* with a 12-hour dark/light cycle. After the acclimation period, a total of $1x10^7$ Env+ cells in 100 μl were injected in the right flank and a week later, $2x10^6$ WT cells in 100 μl were injected in the left flank of either the same mouse or in some cases, in a different animal. Tumors started to develop approximately 2-3 weeks after injection and mice underwent PET imaging when tumors reached a volume of ~300-600 mm^3.

Our study exclusively used female mice primarily to allow for bladder catheterization procedures prior to imaging which could otherwise obscure the signal in the tumors (positioned in the lower flank region). Sex was not considered as a biological variable for this study. Similar findings are expected in male mice.

All experimental procedures, including handling and care of the animals, were performed in an AAALAC International accredited facility. Relevant NIH policies and the Animal Welfare Act and Regulations were followed. The research was approved by the NIH Clinical Center Animal Care and Use Committee.

METHOD DETAILS

Nanobody production and purification

Nanobodies to the HIV-1 gp120 CD4 binding site were developed and published by Laura McCoy and colleagues. Briefly, the J3 and 3E3 nanobodies were isolated from two separate llamas immunized with HIV-1 envelope glycoprotein (Env) in the form of trimeric recombinant gp140 subunits. J3 and 3E3 were then found to neutralize 96 and 82% of tested HIV-1 strains respectively, by targeting the CD4-binding site.[22] The B9 nanobody was subsequently isolated via immunization of llamas with a DNA plasmid encoding gp160 with and without virus like particles bearing the envelope protein and subsequent immunizations with gp140 protein.[36] B9 was found

to neutralize 77% of HIV-1 strains tested.[23] Dr. McCoy provided the plasmids of the three selected nanobodies (J3, 3E3 and B9) for further development as radiotracers at NIH based on their binding and neutralization characteristics.

For further evaluation, purified J3, 3E3 and B9 nanobodies were produced by GenScript (Piscataway, NJ, USA). Briefly, native nanobodies and those with an additional LPETG sortag in the C-terminus (for site-specific labeling by sortagging) were cloned into pET30a plasmids and expressed in the BL21(DE3) *E. coli* strain from which they were purified.

Affinity measurements by bio-layer interferometry (BLI) assay

The binding affinities (K_D value = equilibrium dissociation constant) of nanobodies (J3, LPETG-J3, 3E3, LPETG-3E3, B9, and LPETG-B9) to Fc-gp120 protein (ARP-11556, NIH AIDS Reagent Program) were assessed using an Octet k2 system (Sartorius, Bohemia, NY, USA). We chose Fc-tagged gp120 protein to avoid the use of other gp120 proteins that commonly contain a His tag, as it would have interfered with the loading process of His-tagged nanobodies onto the BLI Nitrilotriacetic acid (NTA) sensors (Cat# Nos.18-5101; Sartorius). The buffer system used consisted of 1X Phosphate buffered saline (PBS) with 0.1% Bovine Serum Albumin (BSA) and 0.02% Tween 20. The NTA biosensors were blocked with 0.1% BSA, after which they were loaded with His-tagged nanobodies (1μg/mL for J3; 4μg/mL for 3E3; 5μg/mL for B9). These sensors were then exposed to gp120 protein of different concentrations (0 to ∼300 nM) and subsequently dipped in PBS to allow for dissociation. Data analysis and fitting of the association and dissociation curves were performed using Octet Analysis Studio 13.0 (Sartorius, Bohemia, NY, USA). The k_{on} and k_{off} values were then used to calculate the K_D values for each nanobody ($K_D = k_{on}/k_{off}$). Four separate measurements were obtained for each nanobody.

Radiolabeling of nanobodies

Non-site specifically labeled nanobodies were prepared by an indirect labeling method using a prosthetic group, 6-fluoronicotinic acid-2,3,5,6-tetrafluorophenyl ester (6-[^{18}F]FPy-TFP), targeting the epsilon amino group of lysine residues to produce [^{18}F]F nanobody ([^{18}F]FJ3, [^{18}F]F3E3, and [^{18}F]FB9).[43]

We also evaluated the use of site-specific labeling, where the radioisotope is linked specifically at the C-terminal of the nanobody, preventing interference with the binding site, using an SrtA conjugation method. SrtA is a transpeptidase derived from *Staphylococcus aureus* that anchors cell wall proteins to the peptidoglycan layer of the bacterial cell.[44] In this radiolabeling approach, the C- or N- terminals of the nanobody are modified through the addition of an LPXTG motif (with X being any amino acid; in this study X is glutamate; LPETG) which can be recognized by SrtA.[27,45,46] Subsequently, SrtA cleaves the polypeptide backbone of the substrate protein at the position where LPXTG was incorporated producing an acyl-enzyme intermediate which is followed by formation of a new peptide bond between the threonine residue in the motif and the N-terminal glycine of a nucleophilic imaging probe.[31] Site-specific labeling of the nanobodies using SrtA conjugation at the C-terminus was performed with an Al[^{18}F]F chelation method to produce Al[^{18}F]F-nanobody.[27]

Competitive binding assays with radiolabeled nanobodies

To validate the BLI results and assess if the radiolabeling procedures induced any alterations to the nanobody binding affinity to gp120 protein, competitive binding assays were performed for [^{18}F]J3 and [^{18}F]Sortag-J3, on Multiscreen® high binding strip plates (Millipore Sigma) coated with 3μg/mL Fc-gp120 protein (ARP-11556, NIH AIDS Reagent Program) or to tubes containing 2x10^5 Env+ HEK293T cells. Briefly, 10 nM of each ^{18}F-labeled nanobody was added in the presence of increasing concentrations of cold nanobodies to the plates coated with gp120 protein (0-500 nM) or to tubes with Env+ cells (0-4000nM).[47] After one-hour incubation at 37°C (gp120 protein) or room temperature (Env+ cells), they were washed with PBS and the wells of plate or tubes with protein/ Env+ cell pellets were collected to measure the radioactivity using a gamma counter (PerkinElmer). Each concentration was run in quadruplicates per assay. The competitive binding curves were plotted, and the best-fit 50% inhibitory concentration (IC50) values were determined using GraphPad Prism 10 software (GraphPad Software, San Diego, CA, USA).

PET/CT imaging and analysis

PET/CT imaging of control mice (no tumors) and mice with flank tumors was performed using the nanoScan imager (Mediso, Budapest, Hungary). The radiotracers (∼7.4 MBq) were injected intravenously into the tail veins of nude mice. A subset of the mice underwent dynamic scanning from the time of tracer injection for a period of 60 minutes followed by a CT scan for attenuation correction and anatomical localization. A static PET/CT scan was performed on all mice two hours after tracer injection. Image reconstruction was done using the 3D ordered subject expectation maximization algorithm (OSEM-3D). Image analysis was conducted by drawing volumes of interest (VOIs) around the tumors using MIM 7.3.3 (MIM software Inc., Beachwood, OH, USA) by at least two operators independently. Quantified ligand binding is represented as SUVmean values for organs. For tumors, we used SUVmean and SUVpeak. The SUVpeak was defined by calculating the mean SUV in a sphere with a diameter of 1 mm within the tumor region with the highest activity. Time activity curves of tumors and various organs were generated from the dynamic and static data.

Immunofluorescence (IF) microscopy

To confirm gp120 expression in HEK293T cells prior to implantation in the flanks of the nude mice, a total of 15,000 cells/well were seeded in 8-well chamber slides in a final volume of 200μl DMEM complete media. Cells were incubated for 24 hours, fixed with 4% paraformaldehyde (PFA), blocked with 5% bovine serum albumin for one hour, and incubated with primary antibody VRC01

(#ARP-12033, NIH AIDS Reagent Program) at a concentration of 2μg/ml overnight at 4°C. The next day, cells were washed 3 times with Tris buffered saline (TBS) for 5 minutes each wash and incubated with secondary antibody, Alexa fluor 647 (cat#21445; Invitrogen, Waltham, MA, USA) at a 1:2000 dilution for one hour at room temperature. Cells were washed 3 times with TBS for 5 minutes each wash, followed by a 5-minute incubation with TrueVIEW autofluorescence quenching reagent following manufacturer's instructions (# SP-8400, Vector Labs). A drop of mounting media containing 4',6-diamidino-2-phenylindole (DAPI) was added per well and cells were protected with a cover slip. Images were taken using a Zeiss Axio inverted microscope (Zeiss, Germany) and gp120 expression was confirmed.

To assess expression of gp120 in tumors following PET/CT scanning, tumors were dissected and fixed in 4% PFA overnight. The tumors were dehydrated in 15% sucrose solution, and then transferred to a 30% sucrose solution until tumors sank to the bottom of the tubes. The sucrose gradients are used to prevent ice crystal formation which could disrupt cellular architecture. Tumors were then embedded in optimal cutting compound (OCT) blocks and stored at -80°C until they were sectioned into 10 μM slices. Sections were thawed at room temperature, incubated in cold acetone for 10 minutes and washed one time with TBS. Subsequently, the tumor sections underwent the same staining procedure as the cells. Besides VRC01 antibody, tumors were also stained with J3, 3E3 and B9 nanobodies at a concentration of 20μg/ml. AlexaFluor 647 anti-His Tag (#362611, Biolegend) was used as the secondary antibody at a 1:1000 dilution. After incubation with the autofluorescence quenching reagent, cell nuclei were counterstained with DAPI at a concentration of 5ug/ml. Tumor sections were imaged using an Olympus VS200 slide scanner (Olympus, Tokyo, Japan).

QUANTIFICATION AND STATISTICAL ANALYSIS

GraphPad Prism 10 software (GraphPad Software, San Diego, CA, USA) was used for statistical analyses. SUV values between groups were compared using 1-way ANOVA or unpaired two-tailed t-tests depending on the experimental design and p-values < 0.05 were considered statistically significant. Additional denotations of statistical significance in the figures are as follow: *$p < 0.05$, **$p < 0.01$, ***$p < 0.001$, ****$p = 0.0001$, ns = not significant. Quantitative data are expressed as mean ± standard deviation (SD) and error bars represent SD unless stated otherwise. Figures and figure legends describe the details of relevant statistical analyses, including types of statistical tests performed and exact animal numbers (n = animal number in each group).